

# Stabilization mechanisms of CH<sub>4</sub> premixed swirled flame enriched with a non-premixed hydrogen injection

D. Laera<sup>a,b,\*</sup>, P. W. Agostinelli<sup>a,c</sup>, L. Selle<sup>b</sup>, T. Schuller<sup>b</sup>, L. Gicquel<sup>a</sup>, T. Poinso<sup>b</sup>

<sup>a</sup>CERFACS, 42 avenue Gaspard Coriolis, 31057 Toulouse, France

<sup>b</sup>IMFT, Allée du Professeur Camille Soula, 31400 Toulouse, France

<sup>c</sup>Safran Helicopter Engines, Bordes, France

---

## Abstract

High-fidelity Large Eddy Simulations (LES) are performed to study the effect of hydrogen injection on a lean turbulent CH<sub>4</sub>/Air premixed flame. To do so, an Analytically Reduced Chemistry (ARC) mechanism is used to achieve a detailed description of CH<sub>4</sub>/Air-H<sub>2</sub> chemistry in the compressible LES solver. First, a validation of this kinetic scheme against the detailed GRI-3.0 mechanism is presented considering both simplified and complex transport properties. The main observation is that when hydrogen is added to the mixture, large variations of the mixture Prandtl and of the N<sub>2</sub> Schmidt numbers are observed depending on the local concentration of H<sub>2</sub>, CH<sub>4</sub> and N<sub>2</sub>, features that are missed by simplified models. LES is then applied to study the structure and stabilization mechanisms of a hydrogen swirled enriched flame by using different transport modeling strategies. First, a lean ( $\phi=0.8$ ) fully premixed CH<sub>4</sub>/Air case is considered with simplified transport and results are found to validate the LES approach. In agreement with experiments, a classical V-shape flame is stabilized in the low-velocity zone near the flame holder and created by the central recirculation zone (CRZ). Then, hydrogen enrichment is achieved injecting 2% of the CH<sub>4</sub> power. Both premixed and diffusion flames are present in this case, impacting flame stabilization and angle. Indeed, at the flame root the main premixed flame is found to be stabilized on a diffusive flame kernel created by the injected hydrogen reacting with the oxygen in excess of the lean premixed stream. Moreover, the H<sub>2</sub> consumed with the remaining oxygen in burnt gasses leads to the formation of a second flame branch inside the CRZ which is responsible of the flame angle increase compared to the fully premixed case. Given the high concentration of hydrogen, an impact of the molecular transport models is observed in this case on the flame lift-off height highlighting the importance of using complex transport properties in any LES involving hydrogen combustion.

## Keywords:

H<sub>2</sub> enriched flame, Flame stabilization mechanism

---

---

\*Corresponding author:

Email address: laera@cerfacs.fr (D. Laera)

## 1. Introduction

Stringent regulations on pollutants emissions applied to combustion devices to comply with EU objectives, make the development of low-emission combustors a major design challenge for aero and land-based gas turbines. In this scenario, the combination of hydrogen with standard carbon-based fuels is actually considered as one of the most promising technical solution for clean combustion [1]. Indeed, lean flame stabilisation is enhanced by the hydrogen high flame speeds [2] and its wide flammability range [3]. Furthermore, hydrogen offers no emissions of HC or CO<sub>2</sub> [4] and NO<sub>x</sub> emissions decrease significantly due to lower global temperatures if compared to richer flames. [5].

For these reasons, multiple numerical and experimental studies have been carried out to study the impact of hydrogen addition on methane/air flames. Experiments and Direct Numerical Simulations (DNS) on laminar flame speeds [6–9], lean and anomalous blow-off [10, 11], stabilization mechanisms and instabilities [12] have been performed for laminar flames. More realistic swirled configurations have been also investigated. Schefer *et al.* [13] experimentally studied the impact of hydrogen on flame stability and blowout maps for a lean premixed swirl-stabilized flame showed that the addition of a moderate amount of hydrogen to the methane/air mixture increased the peak OH concentration with a significant change in the flame structure which is shorter and more robust. A non-premixed unconfined configuration was investigated by Cozzi and Coghe [14]. Fuel mixtures containing a variable volumetric fraction of CH<sub>4</sub> and H<sub>2</sub> are injected in a swirling air flow. Again with hydrogen addition a shorter and narrowed blue flame located closer to the burner head was observed. The impact of H<sub>2</sub> on emissions was also extensively studied. As an example, a decrease of NO<sub>x</sub> level, if compared with a corresponding diffusion flame under same operating conditions, was observed for a fuel-lean confined swirl-stabilized methane-air flame by Kim *et al.* [15]. Recently, the impact of hydrogen enrichment on the shape of a confined swirled flames was experimentally investigated by Guiberti *et al.* [16] and Shanbhogue *et al.* [17]. In both studies, the probability of stabilizing a M-flame increases with the H<sub>2</sub> concentration in the combustible mixture. From a numerical point of view, the appeal of high-fidelity LES (e.g., see Ref. [18]) is increasing for these studies given their higher accurate prediction capabilities at a reasonable cost if compared to cheaper Unsteady Reynolds Averaged Simulations (URANS) and unaffordable DNS. Refs. [19, 20] reports some examples of studies on aca-

demical configurations and, very recently, the methodology was also extended to a full-scale gas turbine combustor [21]. In all these previous studies hydrogen is always considered fully premixed with the fuel mixture. Fewer are the investigations of direct H<sub>2</sub> injection in the combustion chamber. Indeed, in this case the pure H<sub>2</sub> flame will behave as a classical pilot flame typical of land-based gas turbines or aeroengines [1] opening new questions on the resulted flame structure and stabilization mechanisms.

The present work aims to fill the observed gap of knowledge by performing experiments and high-fidelity LES of the impact of H<sub>2</sub> injection on flame structure and stabilization of a confined lean swirling flame. For this specific objective, simulations are performed coupling the LES solver AVBP with an Analytically Reduced Chemistry(ARC) scheme for CH<sub>4</sub>/Air-H<sub>2</sub> chemistry. The impact of considering simplified or complex transport properties is also discussed. This is a topic well developed for classical single-fuel systems, but less investigated in case of bi-fuel configurations [22]. With respect to a classical lean CH<sub>4</sub>/Air premixed swirled flame, simulations reveal that both premixed and diffusion flames are present when hydrogen is injected, impacting flame stabilization mechanisms and angle.

## 2. Experimental setup and Numerical model

The MIRADAS combustor is sketched in Fig. 1(a). A methane/air mixture is well premixed before entering the upstream longitudinal plenum. After being pushed through a radial swirler consisting of eight channels of section area radius of  $r = 2.25$  mm oriented at 15°, the mixture enters the 100 mm long quartz flame tube through an annular gap of inner and outer diameters equal to 6 and 12 mm, respectively. Hydrogen is conveyed directly at the chamber backplane through a 6 mm pilot line passing along the entire axis of the plenum. At the inlet of the combustion chamber, the two fuel lines are separated only by a thin annular lip of 1 mm (Fig. 1(a)). Two operating points are studied in this work. First, a perfectly premixed methane/air mixture with an equivalence ratio of  $\phi = 0.8$  and thermal power of  $P_{th} = 3.96$  kW is considered (case **REF**). Then, in case **PH2** flame is enriched through the pilot line injecting a mass flow of hydrogen corresponding to the 2% of the CH<sub>4</sub> power of case **REF**. More details of the two operative conditions are summarized in Tab. 1. For **PH2**, the methane mass flow rate is slightly changed in order to keep constant the total thermal power. Note that this specific variation is so small that no significant change in the global equivalence ratio is achieved.

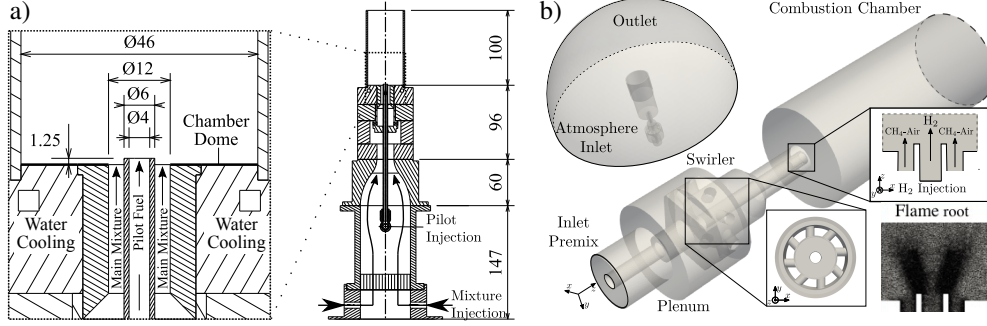


Figure 1: (a) Sketch of the MIRADAS experimental rig. (b) Numerical setup with details of the computational grid at the flame root.

For both cases, in the annular premix passage a well established turbulent flow reaches a Reynolds number of  $Re_{pre,D_h} \approx 7000$  using the equivalent hydraulic radius  $D_h = 1.5$  mm of the annular channel. The hydrogen flow is always laminar and  $Re_{H_2} \approx 25$ .

Case	$\dot{m}_{Air}$ g/s	$\dot{m}_{CH_4}$ g/s	$\dot{m}_{H_2}$ g/s	$\phi$
<b>REF</b>	1.693	7.912E-2	-	0.8
<b>PH2</b>	1.693	7.754E-2	6.597E-4	$\approx 0.8$

Table 1: Different mass flow rates of air, methane and hydrogen and respective global equivalence ratios for the two operative conditions.

The domain used for the LES (Fig. 1(b)) has been discretized using an unstructured mesh which has been refined until a grid-independent solution is obtained. The final computational grid consists of approx. 23M tetrahedral elements. Note that to correctly capture the flame stabilization mechanisms, the grid is designed with a refinement of  $\Delta x \approx 80 \mu m$  in the finest region positioned at the flame root (zoom box in Fig. 1(b)). With this constraint, approximately twelve points are used to resolve the separation zone between the two fuel lines giving at the same time a sufficient resolution of the flame front ( $\Delta_l \approx 550 \mu m$ ) hence avoiding the use of a turbulent combustion model in this specific critical zone. Another refinement region with  $\Delta x \approx 300 - 350 \mu m$  is located further downstream. In this last region, flame thickening is applied using the classical dynamic TFLES model. LES is performed using AVBP (<http://www.cerfacs.fr/avbp7x/>), an explicit cell-vertex parallel code solving compressible reacting flows with the use of the SIGMA turbulent closure for the subgrid Reynolds stresses [23]. A third order accurate Taylor-Galerkin scheme [24] is adopted for discretisation of the convective terms. Inlets and outlets are treated with the Navier-Stokes Characteristic Boundary Conditions [25] imposing the mass flow rates (Tab. 1), and ambient pressure, respectively. For both operating

conditions, a measured temperature of  $T_{bkpl} = 450$  K and  $T_{lip} = 720$  K is fixed, respectively, at the chamber backplane and separator lip. Combustion chamber wall heat losses are taken into account imposing a temperature profile measured with a movable thermocouple from the external side of the flame tube and a thermal resistance of  $R_{w,cc} = 9E - 4$  m<sup>2</sup>K/W computed assuming a conduction coefficient  $\lambda = 2.17$  W/mK for the 2 mm thick quartz wall.

### 3. Chemistry and Transport properties

The CH<sub>4</sub>/Air-H<sub>2</sub> chemistry is described by an ARC mechanism derived from GRI-3.0 comprising 20 species, 166 reactions, and 9 quasi-steady state species [26]. To validate the kinetic schemes, CAN-TERA (<http://www.cantera.org>) calculations of a 1D-counterflow diffusion flame of H<sub>2</sub> against burnt gases from lean CH<sub>4</sub>/Air combustion is presented in Fig. 2. The detailed GRI-3.0 scheme with multicomponent transport and Soret effect [27], is then compared to the reduced ARC mechanisms using both simplified and mixture average transport property models. The latter model is the standard approach for complex transport. Alternatives often present in LES codes are: the simplified approach which consists in determining the viscosity from the Sutherland's law and deducing the mixture heat conductivity using a constant Prandtl number while each species diffusivity relies on a constant Schmidt number. Note that the diffusive flame addressed here is expected to be roughly representative of the H<sub>2</sub> combustion process of the final target configuration. The heat release profiles obtained with the three mechanisms present two reaction peaks, a primary peak in the rich side of the flame, very close to H<sub>2</sub> injection point and the second one, much larger, in the stoichiometric region of the flame (Fig. 2). Normalized species, temperature and

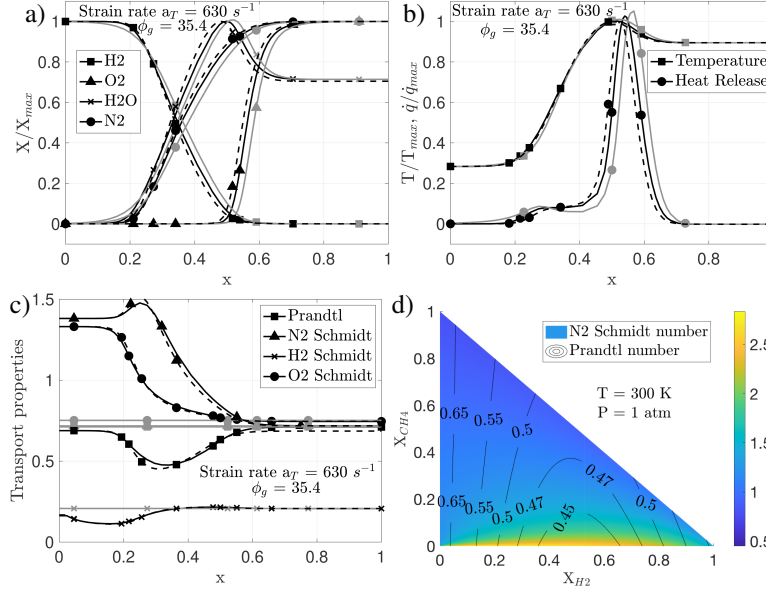


Figure 2: (a-b) Comparison between flame structures computed with Cantera using GRI-3.0 including multicomponent transport and Soret effect (dotted lines), the reduced ARC scheme with a mixture transport model (dark line) and constant transport model (light line), for a H<sub>2</sub> / burnt gases counterflow diffusion flame. Normalized profiles of (a) mass fraction of selected species; (b) temperature and heat release rate are shown. Computation inputs are:  $p = 1$  bar, injection temperature of  $T_{H_2}^i = 570$  K and exhaust gas temperature  $T_g^i = 1800$  K. (c) provides profiles of the transport properties obtained with GRI-3.0 including multicomponent transport and Soret effect (dotted lines), the reduced ARC scheme with mixture transport model (dark line) and constant transport model (light line), for the H<sub>2</sub> / burnt gases counterflow diffusion flame of Figure 2. Finally (d) shows isolines of the Prandtl number and contour map of N<sub>2</sub> Schmidt number in ternary mixture of H<sub>2</sub>, CH<sub>4</sub> and N<sub>2</sub> as a function of composition.

heat release profiles comparison show perfect agreement between GRI-3.0 scheme and the ARC scheme with complex transport while showing only satisfactory agreement with a simplified transport model. Figure 2(c) shows that indeed the Prandtl (Pr) and Schmidt (Sc) numbers of selected species present in the 1D-counterflow diffusion flame confirming the variability present in this problem. Finally, the N<sub>2</sub> Sc and the mixture Prandtl number in a ternary mixture of N<sub>2</sub>, H<sub>2</sub> and CH<sub>4</sub> are reported in Fig. 2(d). It is noted that the GRI-3.0 scheme and the ARC scheme with complex transport predict a Pr number dropping from 0.7 to 0.43 in the region just before the heat release peak, i.e., a region where H<sub>2</sub> and N<sub>2</sub> form a binary mixture of almost equal molar fraction. This leads to higher thermal conductivity and hence to a lower temperature peak in the flame if compared to constant transport property case. By looking at the isolines of the Prandtl number in Fig. 2(d), it can be noticed as Pr is a strong function of the H<sub>2</sub> molar fraction and assumes its minimum values when H<sub>2</sub> is present in a binary mixture with N<sub>2</sub><sup>1</sup> with almost

equal molar fractions. Focusing on the Schmidt number, both the 1D-counterflow diffusion flame of Fig. 2(c) and the ternary mixture of Fig. 2(d) show a variation of the N<sub>2</sub> Schmidt number from 2 when it diffuses in H<sub>2</sub> to only, 0.7 when it diffuses in other gases. Variations of the Schmidt numbers of other species, even if present, do not influence combustion since they are rapidly consumed (e.g. O<sub>2</sub>, CH<sub>4</sub>). Reduced diffusion of N<sub>2</sub> in H<sub>2</sub> due to the increase of Sc, will decrease the local H<sub>2</sub> molar fraction and the resulted flame will be shifted toward the H<sub>2</sub> side. Vice-versa, when simplified transport is used, N<sub>2</sub> will diffuse more in the H<sub>2</sub> side leading to a flame more shifted towards the oxidant side as shown in Fig. 2(b). Relying on these results, variable Pr and N<sub>2</sub> Sc number functions of the molar fraction  $\chi_{CH_4}$ ,  $\chi_{N_2}$  and  $\chi_{H_2}$  are implemented in AVBP and used for the following simulations. These allow to match the complex transport model perfectly for such flames.

<sup>1</sup>It should be also noticed that similar results would have been achieved with a mixture of H<sub>2</sub> with other heavy components such as

O<sub>2</sub>. However, in the present configuration, oxygen is immediately burned either with CH<sub>4</sub> and H<sub>2</sub> so its concentration is extremely low in the zones where hydrogen is present. For this reason, N<sub>2</sub> is considered in Fig. 2(d).

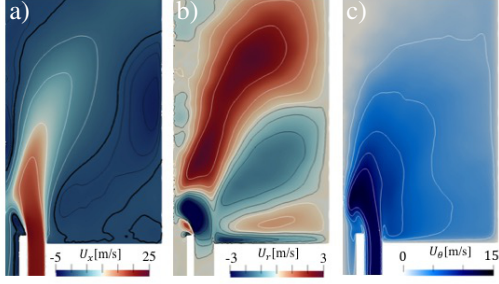


Figure 3: Axial (a), radial (b) and tangential velocity (b) components respectively  $U_x$ ,  $U_r$  and  $U_\theta$ ; time and angle average contours. Black contours indicate negative values, while positive velocities are in white. The tick black line in (a) is  $U_x = 0$ .

#### 4. Results and discussion

Before discussing the reactive simulations, LES time averaged contours of axial  $U_z$ , radial  $U_r$  and tangential  $U_\theta$  velocities in cold flow are shown in Fig. 3(a-c), respectively. note that for this case, the imposed swirl motion is not sufficient to achieve a complete vortex-breakdown: at the exit of the annular channel, a large radial component pushes the jet towards the chamber axis (Fig. 3(b)). As a consequence, the system features a central recirculation zone (CRZ) that is not completely developed as highlighted by the  $U_z=0$  contour (tick black line) in Fig. 3 (a). A good match with experimental results is obtained for global quantities such as the swirl number computed at the entrance of the combustion chamber ( $S_{LES} = 0.35$  against a theoretical value of  $S_{th} = 0.3$ ) and injector head loss ( $\Delta_{p,LES} = 480$  Pa against an experimental value of  $\Delta_{p,exp} = 550$  Pa) confirming the accuracy of the proposed simulations.

##### 4.1. REF case

First, the reactive case **REF**, i.e., with no injected hydrogen (Tab. 1), is discussed. Experimental flame shape obtained taking the line-of-sight (LOS) integration of the  $\text{CH}^*$  chemiluminescence signal is compared in Fig. 4(a-left) with the LOS of the predicted heat release rate Fig. 4(a-right). The predicted global flame shape is in agreement with experiment. As in the experiment, no flame is predicted in the corner recirculation zones (CRZ) proving the appropriateness of the assumed thermal boundary conditions. A good match is also found in terms of lift-off distance and flame angle, whereas LES slightly overestimates the flame total extension. The well-established V-shape of the flame is also clearly visible in Fig. 4(b-left) reporting time and angle average contours of heat release rate. Axial velocity contours are shown in Fig 4(b-right). Comparing

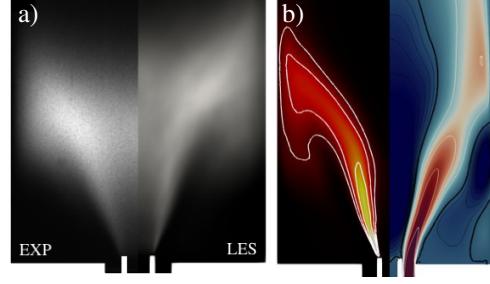


Figure 4: (a) Line-of-sight integration of  $\text{CH}^*$  chemiluminescence (left) and heat release rate  $\dot{q}$   $\text{W/m}^3$  from LES (right) (b) Heat release rate (left) and axial velocity  $U_x$  (right) time and angle average contours. Heat release white contours correspond to values  $\dot{q} = 40, 100, 200 \text{ MW/m}^3$ . For the velocity map, black contours indicate negative values while white contours are for positive velocities and the tick black line refers to  $U_x = 0$ .

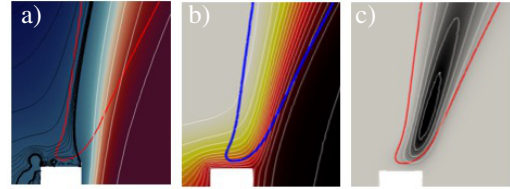


Figure 5: Zoom on the flame root. Contour of heat release rate at 10% of its maximum value ( $\dot{q} = 40 \text{ MW/m}^3$ ) plotted over the contours of (a) axial velocity  $U_x$  m/s, (b) temperature K, (c) mass fraction of  $\text{CH}_3$ .

with the corresponding map for the cold flow, Fig. 3(a) shows that a proper vortex-breakdown with the formation of a complete and extended CRZ is achieved with combustion.

Zooming now at the flame root allows to discuss the flame stabilization mechanisms. An iso-line at the 10% of the maximum of the mean heat release rate (red line) is plotted in Fig. 5 (a) over the axial velocity maps. The swirled flame is stabilized inside the low velocity zone full of hot gases created by the CRZ on top of the separation lip. Plotting the same heat release contour level (in blue for visualization reasons) over the iso-contours of temperature in Fig. 5 (b) underlines the fact that the flame stabilization happens along a temperature value of  $\approx 1300$  K, which is close to the activation temperature of the reaction leading to the production of  $\text{CH}_3$  from methane. Indeed, this specie is found to concentrate within the flame contour (Fig. 5(c)) proving that it is a good indicator of the position of the flame root.

Since no hydrogen is injected, very low  $\chi_{\text{H}_2}$  is obtained for this case (not shown), therefore the impact of the transport model is accordingly negligible.

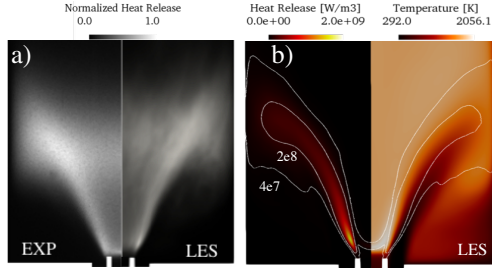


Figure 6: (a) Line of sight integration of experimental light intensity (left) compared with line of sight integration of computed heat release (right). (b) Time and angle average heat release rate. Contours values  $\dot{q} = 40 \text{ MW/m}^3$  and  $200 \text{ MW/m}^3$ .

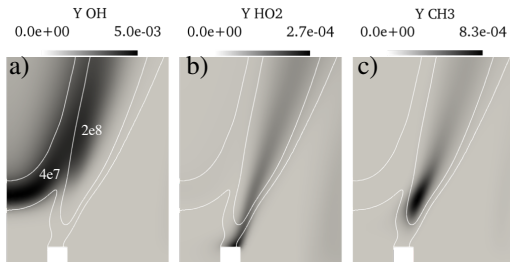


Figure 7: Time average mass fractions of OH, HO<sub>2</sub> and CH<sub>3</sub> with iso-lines of heat release W/m<sup>3</sup>.

#### 4.2. PH2 case

As soon as H<sub>2</sub> is injected from the pilot channel, the flame structure changes (Fig. 6(a)). Focusing on the measurements (right), comparing with the **REF** case (Fig. 6(a-left)), a more intense zone is observed at the flame root and all along the outer side of the flame facing the CRZ. In agreement with the experiments, LES show higher heat release rate in similar areas (Fig. 6 (a-right)). Nevertheless, some differences are observable. A mismatch of approx. 1 mm is indeed noted in the flame lift-off height. This may be due to the lip temperature which was measured in the experiments and imposed in the LES. Time and angle average contours of heat release reported in Fig. 6(b) give more insight on the flame structure. Again, if compared to case **REF**, higher mean values of heat release rate are obtained. The iso-line of heat release rate equal to 10% of the maximum (obtained for  $\dot{q} = 200 \text{ MW/m}^3$ ) shows a flame shape similar to the **REF** case (Fig. 4(b-left)). On the contrary, a flame branch in the CRZ is well detectable by the iso-line at  $\dot{q} = 40 \text{ MW/m}^3$ , i.e, the same level used to indicate the flame in case **REF**. The central region is therefore hotter, with temperature that reaches 2000 K. A wider flame angle is then achieved, in line with experimental observations.

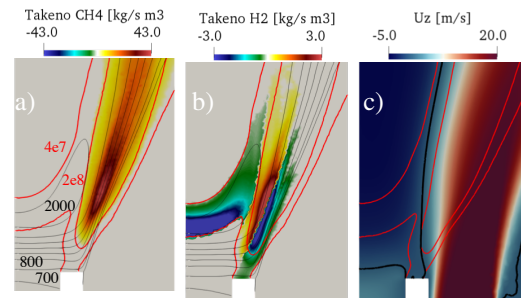


Figure 8: Computed dimensional Takeno of CH<sub>4</sub> (a), dimensional Takeno of H<sub>2</sub> (b) and field of axial velocity (c) with iso-lines of heat release W/m<sup>3</sup> and zero axial velocity line (black thick line). Average (a-b) and Angle average (c) solutions.

Looking at mass fractions of OH, HO<sub>2</sub> and CH<sub>3</sub> in the flame root region, high concentration of OH (Fig. 7(a)) are found to be localized in the heat release isoline  $\dot{q} = 40 \text{ MW/m}^3$  suggesting that the injected H<sub>2</sub> is responsible for the heat release in this zone. Similarly, the presence of high concentration of HO<sub>2</sub> just above the splitter indicates that part of hydrogen is also immediately consumed in that region when the sufficient concentration of H<sub>2</sub> and O<sub>2</sub> is reached (Fig. 7(b)). The high concentration of CH<sub>3</sub> (Fig. 7(c)), instead, indicates that the anchoring point of the CH<sub>4</sub> premixed flame is lifted off with respect to case **REF**. This specie is completely enclosed by the higher  $\dot{q} = 200 \text{ MW/m}^3$  contour confirming that, also for this case, CH<sub>4</sub> oxidation drives the mean heat release.

To better understand the interaction between hydrogen and the premix mixture, two Takeno flame indices (FI) [28] have been computed. To do so, variables are conditioned by the consumption rates of H<sub>2</sub> and CH<sub>4</sub>, respectively, and then weighted by the magnitude of these variables to underline the regions in which heat



release is more relevant:

$$FI_{\text{Fuel}} = |\dot{\omega}_{\text{Fuel}}| \frac{|\nabla_{\text{O}_2} \cdot \nabla_{\text{Fuel}}|}{\left| \left| \nabla_{\text{O}_2} \cdot \nabla_{\text{Fuel}} \right| \right|_{\dot{\omega}_{\text{Fuel}} < 0}} \quad (1)$$

Results in the flame root region are reported in Fig. 8. While the Takeno index of  $\text{CH}_4$  is all positive, indicating that, as expected, it burns in premixed mode (Fig. 8(a)), the FI of  $\text{H}_2$  detects that hydrogen is consumed in both premixed and diffusive regimes (Fig. 8(b)). A large diffusive zone generated by the reaction of  $\text{H}_2$  with residual  $\text{O}_2$  in the burned gasses is found in the CRZ, confirming the hydrogen nature of this second branch of the flame. At the flame root, a premix region is predicted detached from the splitter and is believed to be generated by  $\text{H}_2$  diffusion from the high concentration zone to the  $\text{CH}_4/\text{Air}$  stream. More interestingly, a second diffusive zone is predicted starting from the splitter wall until the premixed zone. This flame is obviously responsible of the  $\text{HO}_2$  concentration previously discussed (Fig. 7(b)) and has a direct role in the stabilization mechanisms of the flame. Indeed, plotting the two heat release isolines over the axial velocity field Fig. 8(c), it is possible to notice that differently from the case **REF**, the hydrogen diffusive flame stabilizes in the low velocity region. This diffusive kernel appears to support the premixed  $\text{CH}_4$  flame that is anchored more downstream in a higher positive velocity region. Observing now the temperature profile (black lines in Fig. 8(a-b)), it is noted that hydrogen oxidation happens in a low temperature zone. The extension of the lower flammability limit temperature is a well-known property of  $\text{H}_2$  that is characterized by reactions at very low activation energy (such as the one correlated to the  $\text{HO}_2$  production). On the contrary, stabilization of the  $\text{CH}_4/\text{Air}$  flames happens at the same temperature value of the **REF** case. ( $T \approx 1300$  K). This shows that the spatial position of the high heat release zone depends on the axial location of these iso-lines which is highly impacted by the Prandtl number of the mixture and the  $\text{N}_2$  Schmidt number as discussed in Sec 3.

Indeed, focusing then on the transport properties, Fig. 9 highlights how the  $\text{Pr}$  (left) and the  $\text{N}_2$   $\text{Sc}$  (right) contours change considerably in the region in which the  $\text{H}_2$  (white lines) molar fraction is relevant. To highlight this result in Fig. 10, an instantaneous snapshot of  $\text{H}_2$  mass concentration of the current simulation (right) is compared with an equivalent instant of a LES calculation performed with simplified transport properties (left). In both images, isolines of the temperature field are also reported (black lines). With complex transport properties (Fig 10(right)) it is noted that

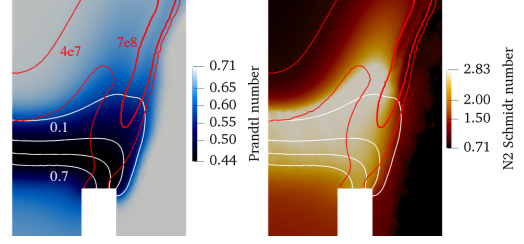


Figure 9: Instantaneous snapshot of Prandtl number (left) and  $\text{N}_2$  Schmidt number (right) with iso-lines of heat release  $\text{W/m}^3$  and  $\text{H}_2$  molar fraction.

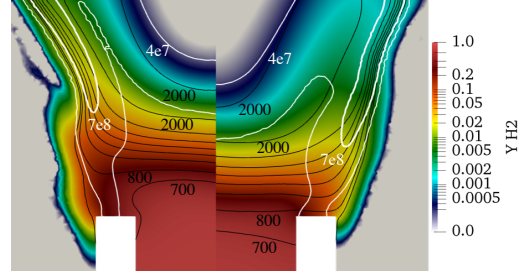


Figure 10: Comparison between constant (left) and complex (right) transport properties computations on an instantaneous snapshot. Mass fraction of  $\text{H}_2$  is shown together with iso-lines of heat release  $\text{W/m}^3$  and temperature K.

the concentration of  $\text{H}_2$  moves upstream since  $\text{N}_2$  diffuses less from the upper region (i.e. higher Schmidt number). Different diffusion of  $\text{H}_2$ , together with the higher thermal conductivity, i.e., lower Prandtl number, has a strong impact on the temperature field, making the hotter region following the movement of  $\text{H}_2$  concentration downward. Simplified transport properties (Fig. 10(left)) fails to correctly reproduce this mechanism, resulting in a less diffuse temperature field. As a consequence, the low-intense hydrogen reaction zone is more stretched and the  $\text{CH}_4$  oxidation is pushed downstream resulting in a lifted flame.

## 5. Conclusions

In this paper, the impact of non-premixed hydrogen addition on the flame shape and stabilization mechanisms of a swirled methane/air flame is proposed by an experimental and numerical analysis. In agreement with experiments,  $\text{H}_2$  injection is found to have a marginal impact on the general flame shape, leading only to a more intense zone at the flame root and all along the outer side of the flame facing the CRZ. On the contrary, both premixed and diffusion flames were discovered by the LES when hydrogen is injected impacting the flame stabilization and its angle. Indeed, at the flame root the

main premixed flame is found to be stabilized on a diffusive flame kernel created by the injected hydrogen reacting with the oxygen in excess of the lean premixed stream. Given the high concentration of  $H_2$  in these regions, LES predictions are found to be influenced by the adopted transport models highlighting the importance of using complex transport properties in any LES involving hydrogen combustion.

## Acknowledgements

This project has received funding from the European Research Council under the European Union's Horizon 2020 research and innovation programme Grant Agreement 832248 (SCIROCCO) from the H2020-MSC-ITN Grant Agreement 766264 (MAGISTER) and from the MSCA-IF Grant Agreement 843958 (CLEANER-FLAMES). This work was performed using HPC resources from GENCI-CINES and CALMIP. Particular gratitude goes to G. Oztarlik from IMFT and Q. Cazerès from CERFACS for providing the experimental data and the ARC mechanism, respectively.

## References

- [1] S. Taamallah, K. Vogiatzaki, F. Alzahrani, E. Mokheimer, M. Habib, A. Ghoniem, Fuel flexibility, stability and emissions in premixed hydrogen-rich gas turbine combustion: Technology, fundamentals, and numerical simulations, *Appl. Energy* 154 (2015) 1020–1047.
- [2] F. Halter, C. Chauveau, N. Djebaïli-Chaumeix, I. Gökalp, Characterization of the effects of pressure and hydrogen concentration on laminar burning velocities of methane-hydrogen-air mixtures, *Proc. Combust. Inst.* 30 (2005) 201–208.
- [3] Y. Zhang, J. Wu, S. Ishizuka, Hydrogen addition effect on laminar burning velocity, flame temperature and flame stability of a planar and a curved  $CH_4$ - $H_2$ -air premixed flame, *Int. J. Hydrogen Energy* 34 (2009) 519–527.
- [4] H. Guo, G. J. Smallwood, F. Liu, Y. Ju, Ö. L. Gülder, The effect of hydrogen addition on flammability limit and  $NO_x$  emission in ultra-lean counterflow  $CH_4$ /air premixed flames, *Proc. Combust. Inst.* 30 (2005) 303–311.
- [5] F. H. Coppens, J. De Ruyck, A. A. Konnov, Effects of hydrogen enrichment on adiabatic burning velocity and  $NO$  formation in methane + air flames, *Exp. Therm. Fluid Sci.* 31 (2007) 437–444.
- [6] V. Di Sarli, A. D. Benedetto, Laminar burning velocity of hydrogen-methane/air premixed flames, *Int. J. Hydrogen Energy* 32 (2007) 637–646.
- [7] Z. Chen, Effects of hydrogen addition on the propagation of spherical methane/air flames: A computational study, *International Journal of Hydrogen Energy* 34 (2009) 6558–6567.
- [8] T. Boushaki, Y. Dhué, L. Selle, B. Ferret, T. Poinso, Effects of hydrogen and steam addition on laminar burning velocity of methane-air premixed flame: Experimental and numerical analysis, *International Journal of Hydrogen Energy* 37 (2012) 9412–9422.
- [9] A. Cuoci, A. Frassoldati, T. Faravelli, E. Ranzi, Extinction of laminar, premixed, counter-flow methane/air flames under unsteady conditions: Effect of  $H_2$  addition, *Chem. Eng. Sci.* 93 (2013) 266–276.
- [10] C. Jiménez, D. Michaels, A. F. Ghoniem, Stabilization of ultra-lean hydrogen enriched inverted flames behind a bluffbody and the phenomenon of anomalous blowoff, *Combust. Flame* 191 (2018) 86–98.
- [11] Y. J. Kim, B. J. Lee, H. G. Im, Hydrodynamic and chemical scaling for blow-off dynamics of lean premixed flames stabilized on a meso-scale bluff-body, *Proc. Combust. Inst.* 37 (2019) 1831–1841.
- [12] X. Kang, R. J. Gollan, P. A. Jacobs, A. Veeraragavan, Suppression of instabilities in a premixed methane/air flame in a narrow channel via hydrogen/carbon monoxide addition, *Combust. Flame* 173 (2016) 266–275.
- [13] R. Schefer, D. Wicksall, A. Agrawal, Combustion of hydrogen-enriched methane in a lean premixed swirl-stabilized burner, *Proc. Combust. Inst.* 29 (2002) 843–851.
- [14] F. Cozzi, A. Coghe, Behavior of hydrogen-enriched non-premixed swirled natural gas flames, *Int. J. Hydrogen Energy* 31 (2006) 669–677.
- [15] H. S. Kim, V. K. Arghode, M. B. Linck, A. K. Gupta, Hydrogen addition effects in a confined swirl-stabilized methane-air flame, *Int. J. Hydrogen Energy* 34 (2009) 1054–1062.
- [16] T. Guiberti, D. Durox, P. Scoufflaire, T. Schuller, Impact of heat loss and hydrogen enrichment on the shape of confined swirling flames, *Proc. Combust. Inst.* 35 (2015) 1385–1392.
- [17] S. Shanbhogue, Y. Sanusi, S. Taamallah, M. Habib, E. Mokheimer, A. Ghoniem, Flame macrostructures, combustion instability and extinction strain scaling in swirl-stabilized premixed  $CH_4/H_2$  combustion, *Combust. Flame* 163 (2016) 494–507.
- [18] P. Benard, V. Moureau, G. Lartigue, Y. D'Angelo, Large-Eddy Simulation of a hydrogen enriched methane/air meso-scale combustor, *Int. J. Hydrogen Energy* 42 (2017) 2397–2410.
- [19] D. Cicoria, C. Chan, Large eddy simulation of lean turbulent hydrogen-enriched methane-air premixed flames at high Karlovitz numbers, *Int. J. Hydrogen Energy* 41 (2016) 22479–22496.
- [20] R. Mercier, T. Guiberti, A. Chatelier, D. Durox, O. Gicquel, N. Darabiha, T. Schuller, B. Fiorina, Experimental and numerical investigation of the influence of thermal boundary conditions on premixed swirling flame stabilization, *Combust. Flame* 171 (2016) 42–58.
- [21] D. Moëll, D. Lörstad, X.-S. Bai, LES of Hydrogen Enriched Methane/Air Combustion in the SGT-800 Burner at Real Engine Conditions, in: *Asme Turbo Expo 2018*, Paper No: GT2018-76434.
- [22] R. Hilbert, F. Tap, H. El-Rabii, D. Thévenin, Impact of detailed chemistry and transport models on turbulent combustion simulations, *Prog. Energy Combust. Sci.* 30 (2004) 61–117.
- [23] F. Nicoud, H. B. Toda, O. Cabrit, S. Bose, J. Lee, Using singular values to build a subgrid-scale model for large eddy simulations, *Phys. Fluids* 23 (2011) 85106.
- [24] O. Colin, M. Rudgyard, Development of high-order Taylor-Galerkin schemes for LES, *J. Comput. Phys.* 162 (2000) 338–371.
- [25] T. J. Poinso, S. Lele, Boundary conditions for direct simulations of compressible viscous flows, *J. Comput. Phys.* 101 (1992) 104–129.
- [26] A. Felden, L. Esclapez, E. Riber, B. Cuenot, H. Wang, Including real fuel chemistry in LES of turbulent spray combustion, *Combust. Flame* 193 (2018) 397–416.
- [27] J. F. Grac, J. B. Bell, M. S. Day, The Soret effect in naturally propagating, premixed, lean, hydrogen/air flames, *Proc. Com-*



- bust. Inst. 32 (2009) 1173–1180.
- [28] H. Yamashita, M. Shimada, T. Takeno, A numerical study on flame stability at the transition point of jet diffusion flames, Symp. Combust. 26 (1996) 27–34.